Interface–induced enhancement of piezoelectricity in $(SrTiO_3)_m$/$(BaTiO_3)_{M-m}$ superlattice for energy harvesting applications

Guntars Zvejnieks,[*a] Leonid L. Rusevich,[a] Denis Gryaznov,[a] and Eugene A. Kotomin[a,b]

We present the results of detailed first principles study of the piezoelectric properties of $(SrTiO_3)_m$/$(BaTiO_3)_{M-m}$ heterostructure using 3D STO_m/BTO_{M-m} superlattice model. The atomic basis set, hybrid functionals and slabs with different number of STO and BTO layers were used. The interplay between ferroelectric (FE_z) and antiferrodistortive (AFD_z) displacements is carefully analyzed. Based on the experimental data and group theoretical analysis, we deduce two possible space groups of tetragonal symmetry which allow us to reproduce experimentally known pure STO and BTO bulk phases in the limiting cases, and to model the corresponding intermediate superlattices. The characteristic feature of the space group $P4mm$ (#99) model is atomic displacements in the $[001]$ direction, that allows us to simulate the FE_z displacements, whereas the $P4$ (#75) model besides FE_z displacements permits oxygen octahedra antiphase rotations around $[001]$ direction and thus AFD_z displacements. Our calculations demonstrate that for $m/M \leq 0.75$ layer ratios both models show similar geometries and piezoelectric constants. Moreover, both models predict approximately 6-fold increase of the piezoelectric constant e_{33} compared to the $BaTiO_3$ bulk value, albeit at slightly different layer ratios. Obtained results clearly demonstrate that piezoelectricity arise due to a coordinated collective FE_z displacements of atoms in both STO and BTO slabs and interfaces and reaches maximum when superlattice approaches the point where tetragonal phase becomes unstable and transforms to a pseudo-cubic phase. We demonstrate that even a single or double layer of BTO is sufficient to trigger a FE_z displacements in STO slab, in $P4mm$ and $P4$ models, respectively.

1 Introduction

Development of effective energy harvesting devices requires search for a new energy conversion materials[1,2]. For a very long time, lead-zirconate-titanate (PZT) perovskite was the most widely used piezoelectric material for electromechanical applications[3]. In recent years, alternative lead-free perovskites were sought for PZT replacement[4]. Potential candidates are $BaTiO_3$-based piezoelectrics[5] whose performance, however, is worse compared to PZT. As we have shown recently[6–8], the $(Ba,Sr)TiO_3$ solid solutions considerably improve piezoelectric properties. However, the main problem here is quite limited Sr concentrations that could be added to $BaTiO_3$ without transition to paraelectric cubic phase. In this paper, we performed first principles study of the $(SrTiO_3)_m$/$(BaTiO_3)_{M-m}$ (hereafter STO_m/BTO_{M-m})

superlattice which is free from this limitation. Moreover, the Curie temperature of STO_m/BTO_{M-m} superlattice could be altered considerably depending on composition comparing to a bulk BTO[9].

Numerous experimental studies were performed recently on STO/BTO superlattices[10–15]. These studies, starting with Tabata *et al.*[16], were motivated by very high dielectric constants of superlattices, in a comparison with the pure constituent materials. Later O'Neill *et al.*[17,18] proposed that the high dielectric constants, at least for fine superlattice structures, can be attributed to Maxwell-Wagner relaxation, i.e. they are an artifact of increased interfacial polarization (increased carrier mobility) rather than relaxor type of behavior (engineered nanoscale heterogeneities). Most of superlattice studies focused on the ferroelectric rather piezoelectric properties.

The symmetry of STO_m/BTO_{M-m} superlattice is quite complicated and, in general, depends on the number of STO and BTO layers, temperature, substrate induced strain, and the total thickness of superlattice. Experimental studies of STO/BTO superlattices could be separated into two groups depending on STO slab

a Institute of Solid State Physics, University of Latvia, Kengaraga Str. 8, LV-1063 Riga, Latvia.

b Max Planck Institute for Solid State Research, Heisenberg str. 1, Stuttgart D-70569, Germany.

* Corresponding author. E-mail: guntars.zvejnieks@cfi.lu.lv

symmetry at ambient temperatures: (i) for STO_m/BTO_m superlattices grown on the STO (001) substrate, STO slabs were found to be orthorhombic ($mm2$) for $m \leq 30$ with a polar axis parallel to [110] and [1$\bar{1}$0] pseudo-cubic directions[19,20]. STO becomes centrosymmetric above critical thickness of 30 unit cells and STO slabs with $m = 10$ and 30 layers transform from orthorhombic to tetragonal and centrosymmetric phase at elevated Curie temperatures of $T_c = 540$ and 599 K[19,20], respectively. In these experiments it was initially proposed that at ambient temperatures BTO slabs have orthorhombic symmetry[19], while later it was clarified[20] that BTO phase has a tetragonal symmetry with a polarization along the [001] direction. Orthorhombic STO slabs were found also in $[STO_4/BTO_8]_{40}$ superlattice on the $SmScO_3$ (110) substrate with Curie temperature $T_c = 660$ K[21].

Alternatively, (ii) STO slab within the STO_m/BTO_m superlattice on the STO (100) (with $m = 1 - 250$)[16,22], MgO (100) (with $m = 1 - 125$)[22–24], MgO (001) (with $m = 6 - 10$)[25] could be tetragonal and ferroelectric, with the polar axis along the surface normal. It was also demonstrated that the tetragonal phase for STO_{10}/BTO_{10} superlattice remains stable down to 77 K, while the phase transition to the paraelectric state is diffused and shifted up to $T_c = 650 - 700$ K[25]. Lastly, the very recent study[14] claims that strained $[STO_4/BTO_8]_{50}$ superlattice on the $DyScO_3$ (110) has the tetragonal $P4mm$ symmetry below 550 K (another phase transition between 200 and 300 K was also suggested[14]).

Thus, tetragonal phase of STO (cubic bulk STO lattice constant 3.905 Å) is stabilized, if STO slabs are in-plane tensilely strained, while BTO slabs (in-plane tetragonal bulk lattice constant 3.992 Å) are compressively strained, e.g., on the $DyScO_3$ (110) (with almost perfect square lattice with parameters 3.946 and 3.952 Å)[14]. Contrary, orthorhombic STO slab phase dominates, if STO slabs experience strong tensile in-plane strain, while BTO are almost unstrained, e.g., for superlattices on the $SmScO_3$ (110) (surface lattice constant 3.987 Å)[21].

Synthesis of the high quality defect-free superlattices are far from trivial. As demonstrated in Refs.[11,12,26,27] using reflection high-energy electron diffraction (RHEED)-assisted laser molecular beam epitaxy (MBE) and conventional MBE from elemental sources, even a single BTO layer in $[STO_{30}/BTO_1]_{20}$ strained superlattice grown on the STO (001) substrate forms a commensurate ferroelectric superlattice. When this superlattice is grown on STO substrate, the STO slabs are unstrained, but become polar due to neighboring BTO layer[12,26]. On different substrates, e.g., $DyScO_3$, $GdScO_3$, or $SmScO_3$, the STO slabs are not only polar, but become strained and exhibit also strain-induced ferroelectricity[26]. Moreover, tetragonality and polarity of BTO and STO slabs within the superlattice where suggested in Ref. 12 along with the concerted mechanism of a transition to paraelectric state (polarization in STO slabs disappears with BTO paraelectricity).

Theoretical studies of STO_m/BTO_{M-m} superlattices are quite extensive. Using first-principles calculations, it was shown[28] that for a tetragonal symmetry ($P4mm$) the polarization is a function of the ratio of the STO/BTO layers and it exceeds the bulk BTO value, if a fraction of BTO in the superlattice exceeds 40%.

It has been demonstrated theoretically[29] using monoclinic symmetry (Cm) that experimentally observed in-plane polarization[19,20] in STO/BTO superlattice are developed only in $SrTiO_3$ slab while polarization in the [001] direction is nearly uniform.

The ultrashort period superlattice BTO_1/STO_1 was studied theoretically[30] using first-principles calculations. It was found that either tetragonal ($P4mm$) or monoclinic (Cm) phase is stable under compressive or tensile in-plane strain, respectively, while orthorhombic phase is unstable irrespective of the applied strain. Polarization is increasing with strain and directed along the [001]-in tetragonal structure, or rotates towards the [110] direction in a monoclinic phase, respectively.

Similarly, detailed studies[31] have shown that the unstrained BTO/STO superlattice ground state is a polar monoclinic phase (Cm), and a compressive in-plane strain stabilizes the tetragonal ($P4mm$) phase. Contrary to Ref. 30, Lebedev[31] argues that orthorhombic ($Amm2$) phase should be observed for tensile in-plane strain[31]. Moreover, he studied in detail spontaneous polarization, dielectric, piezoelectric, and elastic properties of short period STO_1/BTO_1 superlattice depending on in-plane strain[31]. Polarization properties of short period superlattices were studied also in Ref. 32.

The motivation for the current research was to find the optimal structural composition of STO/BTO superlattice that promises the enhanced piezoelectric properties suitable for energy harvesting and other applications. Our model neglects the effect of substrate-induced strain and considers fully relaxed superlattice of infinite periodicity $[STO_m/BTO_{M-m}]_\infty$ (below we omit periodicity abbreviation). We consider the lowest symmetry of the superlattice to be tetragonal, that allows us to reproduce the experimentally well established phases of perovskites in the limiting cases of pure bulk STO and BTO perovskites.

2 Superlattice models

As discussed above, the experimental information regarding symmetry of the STO_m/BTO_{M-m} superlattice varies considerably, mainly suggesting different STO phases, starting from tetragonal to orthorhombic (and monoclinic in the first principles calculations[29–31]). We limit our superlattice model to the tetragonal symmetry as suggested in recent experiment studies[12–14] and develop a model on the basis of the space-group symmetry relations.

We require that STO_m/BTO_{M-m} model in the limiting cases of bulk STO and BTO crystals reproduces experimentally established symmetries $Pm\bar{3}m$ or $I4/mcm$ for STO (above/below below 105 K) and $Pm\bar{3}m$ or $P4mm$ for BTO (above/below 396 K). To this end, let us build the Bärnighausen group–maximal subgroup tree,[34] Fig. (1), starting from the cubic $Pm\bar{3}m$ *aristotype* structure of both STO and BTO high temperature phases up till lowest possible tetragonal phase $P4$ using Bilbao Crystallographic Server[35].

Upon transformation from supergroup to its maximal subgroup, the kind (*translationengleiche* (t) or *klassengleiche* (k)) and index of the subgroup is given next to the corresponding arrow in Fig. (1). If subgroup basis vectors change, the transformation is given in the terms of the corresponding supergroup basis vectors. Dashed lines indicate that alternative route of transformation exists. The fixed coordinates of atom Wyckoff positions are given as fractions, while free to change coordinates are given as displacements, δ, from the corresponding pseudo-cubic structure coordi-

$Pm\bar{3}m$ (#221)

STO(>105K), BTO(>396K)

t3 ↓

$P4/mmm$ (#123)

k2 **a−b, a+b, 2c** ↙   ↘ t2

$I4/mcm$ (#140) $P4mm$ (#99)

STO(<105K)   BTO(>278K)

t2 ↓   k2 **a, b, 2c** ↘

$I4cm$ (#108) $P4mm$ (#99)

t2 ↓   k2 **a−b, a+b, c** ↓

$I4$ (#79) $P4mm$ (#99)

k2 ↘   t2 ↙

$P4$ (#75)

$Pm\bar{3}m$		
A:1b	Ti:1a	O:3d
$m\bar{3}m$	$m\bar{3}m$	$4/mm.m$
1/2	0	1/2
1/2	0	0
1/2	0	0

$P4/mmm$			
A:1d	Ti:1a	O_I:1b	O_{II}:2f
$4/mmm$	$4/mmm$	$4/mmm$	$mmm.$
1/2	0	0	1/2
1/2	0	0	0
1/2	0	1/2	0

$P4mm$			
A:1b	Ti:1a	O_I:1a	O_{II}:2c
$4mm$	$4mm$	$4mm$	$2mm.$
1/2	0	0	1/2
1/2	0	0	0
$0.5+\delta$	δ	$0.5+\delta$	δ

$I4/mcm$			
A:4b	Ti:4c	O_I:4a	O_{II}:8h
$\bar{4}2m$	$4/m..$	422	$m.2m$
0	0	0	$0.25+\delta^a$
1/2	0	0	$0.25-\delta^a$
1/4	0	1/4	0

^{a} Alternative setting is possible using $\delta = 0.25 - \delta'$.

Enlarged $P4mm$					
A:$2c_1$	A:$2c_2$	Ti:$1a_1$	Ti:$1a_2$	Ti:$1b_1$	Ti:$1b_2$
$2mm.$	$2mm.$	$4mm$	$4mm$	$4mm$	$4mm$
0	0	0	0	1/2	1/2
1/2	1/2	0	0	1/2	1/2
$0.25+\delta$	$0.75+\delta$	δ	$0.5+\delta$	δ	$0.5+\delta$
O_I:$1a_1$	O_I:$1a_2$	O_I:$1b_1$	O_I:$1b_2$	O_{II}:$4d_1$	O_{II}:$4d_2$
$4mm$	$4mm$	$4mm$	$4mm$	$..m$	$..m$
0	0	1/2	1/2	$0.25+\delta_x$	$0.25+\delta_x$
0	0	1/2	1/2	$0.25+\delta_x$	$0.25+\delta_x$
$0.25+\delta$	$0.75+\delta$	$0.25+\delta$	$0.75+\delta$	δ_z	$0.5+\delta_z$

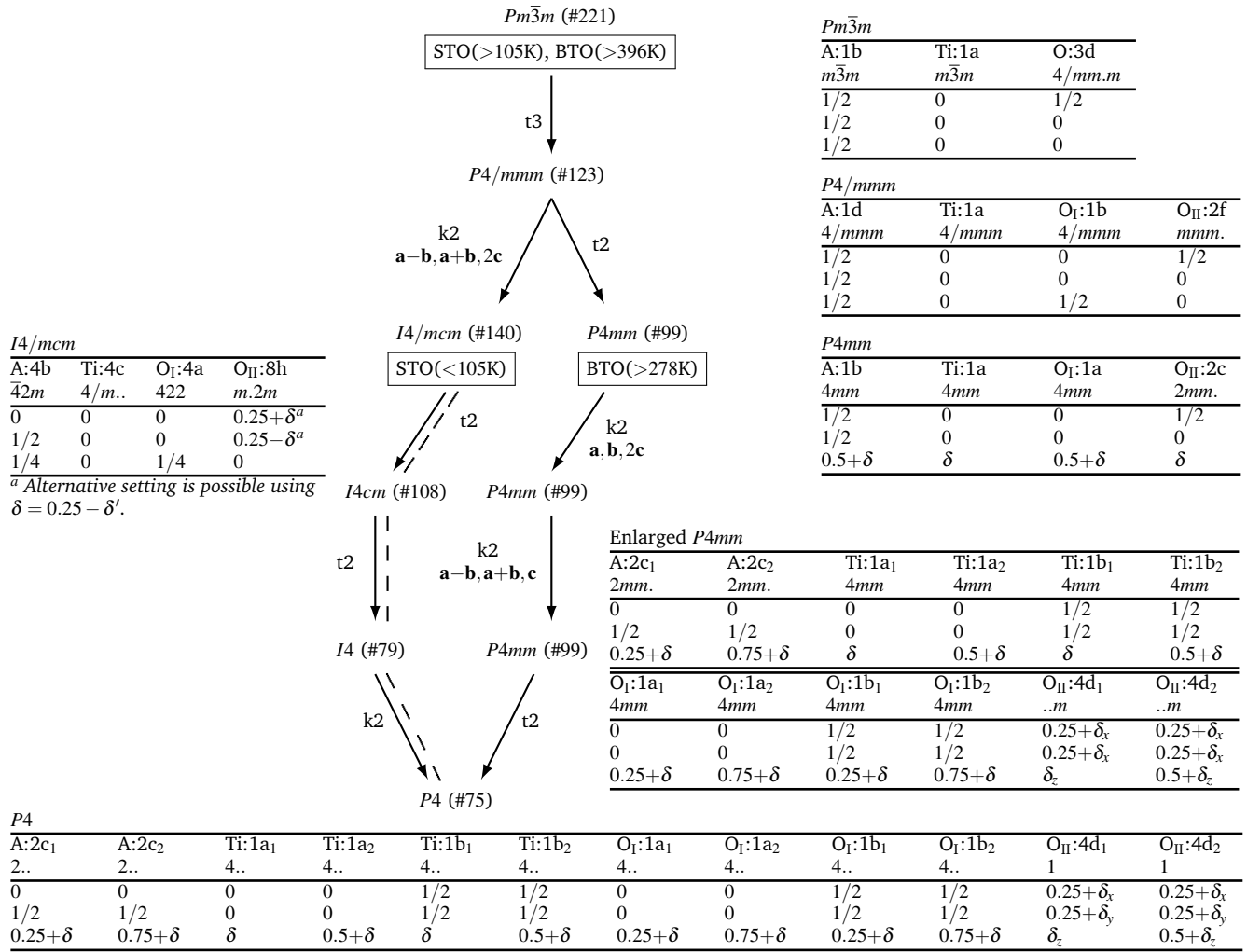| $P4$											
A:$2c_1$	A:$2c_2$	Ti:$1a_1$	Ti:$1a_2$	Ti:$1b_1$	Ti:$1b_2$	O_I:$1a_1$	O_I:$1a_2$	O_I:$1b_1$	O_I:$1b_2$	O_{II}:$4d_1$	O_{II}:$4d_2$
$2..$	$2..$	$4..$	$4..$	$4..$	$4..$	$4..$	$4..$	$4..$	$4..$	1	1
0	0	0	0	1/2	1/2	0	0	1/2	1/2	$0.25+\delta_x$	$0.25+\delta_x$
1/2	1/2	0	0	1/2	1/2	0	0	1/2	1/2	$0.25+\delta_y$	$0.25+\delta_y$
$0.25+\delta$	$0.75+\delta$	δ	$0.5+\delta$	δ	$0.5+\delta$	$0.25+\delta$	$0.75+\delta$	$0.25+\delta$	$0.75+\delta$	δ_z	$0.5+\delta_z$

Fig. 1 Space-group – maximal subgroup relation tree for STO and BTO perovskites in a cubic and tetragonal symmetries. The coordinate origin shift is absent in all transformations, while dashed line indicate the existence of alternative routes. Wyckoff positions for (A)TO, where A=S or B, atoms in $Pm\bar{3}m$, $P4/mmm$, $I4/mcm$, $P4mm$, enlarged $P4mm$ and $P4$ are given in tables. Atom fractional coordinates (x,y,z) are given as columns, where δ denote displacements from pseudo-cubic $Pm\bar{3}m$ positions, that are free to change. In different columns δ values are independent, while for different δ values in a single column different subscripts are used. Experimentally determined temperature of the phase stability is given in brackets[33].

nates given as decimals. We provide information in framed boxes, for experimentally known STO and BTO phases along with their temperature limits.

In a cubic ATO perovskite structure $Pm\bar{3}m$ (where A stands for either Sr(S) or Ba(B)) atoms could be placed in one of two alternative Wyckoff positions: (a) A:1b, Ti:1a, O:3d or (b) A:1a, Ti:1b, O:3c, respectively, that differ by $(\frac{1}{2}, \frac{1}{2}, \frac{1}{2})$ origin shift. Let us now consider STO in $Pm\bar{3}m$ symmetry, where transition to lower tetragonal $I4/mcm$ phase is driven by antiferrodistortive instability mode at R-point[36]. The STO transition to tetragonal $I4/mcm$ phase with experimentally detected Wyckoff positions S:4b, Ti:4c, O_I:4a, O_{II}:8h[37] without coordinate origin change is possible only from Wyckoff position set (a), to be used in this paper. In the $I4/mcm$ structure the antiphase rotation of neighboring TiO$_6$ oxygen octahedra around the [001] axis is described by a single free parameter δ, i.e., antiferrodistortive displacements (AFD$_z$) of O_{II} in Wyckoff positions 8h from their cubic positions, see Figs. 1 and 2a.

A BTO from a cubic $Pm\bar{3}m$ phase transforms to a tetragonal

$P4mm$ one due to ferroelectric instability mode at the Γ-point[38]. Druing this step Wyckoff position set (a) splits to Ba:1b, Ti:1a, O_I:1a and O_{II}:2c, see Fig. 1 (in agreement with experimentally determined set Ba:1a, Ti:1b, O_I:1b and O_{II}:2c[39] due to equivalency of these Wyckoff positions). Geometrically this corresponds to atom relaxation along the [001] direction, i.e., ferroelectric displacements (FE$_z$), see Fig. 2a. This relaxation leads to the loss of center of inversion and appearance of piezoelectric and ferroelectric properties in tetragonal $P4mm$ BTO.

In general three tetragonal STO/BTO superlattice models are possible, that in the limiting cases of pure STO and BTO would lead to the above considered perovskite phases. Two superlattice models could be constructed straightforwardly on the basis of $P4mm$ or $I4/mcm$ symmetries, respectively. (i) Within the $P4mm$ model FE$_z$ displacements and piezoelectric behavior is allowed by symmetry. Here oxygen octahedra rotation, i.e., AFD$_z$ displacements is absent, see Fig. 1. (ii) Within the $I4/mcm$ model only AFD$_z$ displacements are allowed, see Figs. 1. However, FE$_z$ displacements and thus piezoelectric effects in this model are absent

due to existence of center of inversion.

(iii) In order to built a general model that combines both FE_z and AFD_z displacements, let us increase the original $P4mm$ unit cell size

$$P4mm \; (99) \rightarrow \mathrm{k2} \; (\mathbf{a},\mathbf{b},2\mathbf{c}) \rightarrow P4mm \; (99) \rightarrow$$

$$\mathrm{k2} \; (\mathbf{a}-\mathbf{b},\mathbf{b}+\mathbf{b},\mathbf{c}) \rightarrow P4mm \; (99), \qquad (1)$$

firstly, by doubling it in the $\mathbf{c}$ direction and, secondly, by a rotation and increase along the $\mathbf{a}$ and $\mathbf{b}$ basis vectors, that could be described by a transformation matrix $\left(\begin{smallmatrix} 1 & 1 & 0 \\ \bar{1} & 1 & 0 \\ 0 & 0 & 2 \end{smallmatrix} \right)$. The corresponding splitting of Wyckoff positions for the enlarged $P4mm$ are given in Fig. (1). The x and y coordinates of O_{II}:4d are free to change, however, still in a constrained $\delta_x = \delta_y$ manner, that allows no rotation of oxygen octahedra as in $I4/mcm$. Further reduction of symmetry to $P4$ is required to obtain a single superlattice model that in the limiting cases of bulk STO and BTO crystals leads to $I4/mcm$ and $P4mm$ symmetries, respectively.

Thus, the symmetry considerations allow us to choose two tetragonal STO_m/BTO_{M-m} superlattice models for a further piezoelectric property studies (i) $P4mm$ with FE_z displacements and (iii) $P4$ with both FE_z and AFD_z displacements.

3 Computational details

The first-principles calculations were performed using the CRYSTAL17[40,41] computer code within the density–functional theory (DFT) formalism. The single particle wave functions are expanded as a linear combination of Bloch functions that, in turn, are linear combination of atomic orbitals (Gaussian type functions). For O atom we use all-electron basis sets[42], while for Ti, Sr and Ba atoms – the Hay and Wadt small core effective core pseudo-potentials (ECP)[43].

We used a single parameter hybrid exchange-correlation functional B1WC, that combines Wu and Cohen (GGA-WC) exchange functional with 16% of HF exchange and the Perdew–Wang (PWGGA) correlation functional[41,44]. B1WC was designed to improve the calculated electronic and structural properties of prototypical oxides[44].

To calculate the piezoelectric properties of STO_m/BTO_{M-m} superlattices, we consider two tetragonal models, based either on $P4mm$ symmetry with 5 atoms (a single layer) per unit cell, or $P4$ – with 20 atoms (two layers) per unit cell. The STO_m/BTO_{M-m} superlattices with a total number (period) of $M = 8$, 16 and 32 layers are created containing also a different number, m, of STO and, $M - m$, BTO layers. The periodic boundary conditions in 3D are imposed on the lattice, see Fig. 2a. The limiting cases of pure bulk STO and BTO perovskites within $Pm\bar{3}m$, $I4/mcm$, $P4mm$, and $P4$ symmetries are also considered.

For $I4/mcm$ and $P4$ we use $6 \times 6 \times N$ Monkhorst-Pack k-point mesh, while for $Pm\bar{3}m$ and $P4mm$ – $8 \times 8 \times N$ Monkhorst-Pack k-point mesh[45]. In bulk $I4/mcm$ and $P4$ cases we used $N = 6$ and 4, respectively, while for $Pm\bar{3}m$ and $P4mm$ cases $N = 8$. For all superlattices we set $N = 1$, independently on a total number of layers, M. Exceptions are superlattices that are build on $I4/mcm$ model, where we set $N = 6$, due to primitive cell type used in CRYSTAL
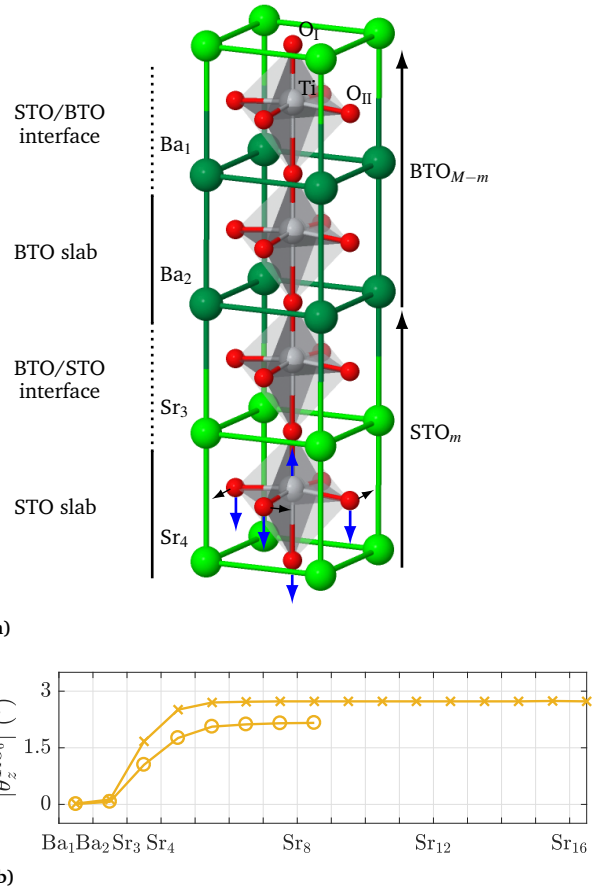

(a)

(b)

Fig. 2 (a) Schematic view of a fraction of STO_m/BTO_{M-m} superlattice (Ti-grey, O-red, Ba-dark green, Sr-light green). FE_z and AFD_z displacements are marked with blue and black arrows, respectively. (b) Modules of oxygen octahedra rotation angles, $\theta_z^{TiO_6}$, in the $P4$ model for $m/M = 14/16$ (circles) and $30/32$ (crosses) superlattices.

calculations.

Tolerances for Coulomb and exchange sums are set to 8 8 8 8 16, while SCF convergence threshold on total energy – to 10^{-10} hartree[41]. Integration is performed on a predefined pruned grid consisting of 99 radial and maximum of 1454 angular points (XXL-GRID) (in order to achieve accurate convergence of geometry that is required for piezocoefficient estimates); DFT density and DFT grid weight tolerances are kept as 9 and 18, respectively; for SCF convergence acceleration Fock/KS matrices mixing percentage (FMIXING) is set to 60 and Anderson's method (ANDERSON) is used; pseudo-potential tolerance (truncation criteria for integrals involving ECPs) are set to 10; maximum order of multipolar expansion set to 6 (POLEORDR[41].

Full geometry optimization was performed provided the energy difference between two steps threshold (TOLDEE) is less than 10^{-10} hartree, and the root-mean-square of the gradient (TOLDEG) and displacement (TOLDEX) is 0.00003 hartree/bohr and 0.00012 bohr, respectively, using no trust radius to limit displacement (NOTRUSTR).

First-order direct piezoelectric constant, e_{33}, describes the polarization P in [001] direction induced by strain along the same

[001] direction, η, at a constant electric field [41,46]

$$e_{33} \cong \left(\frac{\partial P}{\partial \eta}\right)_E, \qquad (2)$$

where Voigt's notations are used. In order to calculate the *proper direct piezoelectric constant*, e_{33}, we use the Berry phase, φ, (BP) approach [41,47] within the framework of the modern theory of polarization. Then the piezoelectric constant is calculated as a numerical derivative of the BP projection along the [001] direction, φ, with respect to strain, η,

$$e_{33} = \frac{|e|}{2\pi V} c \frac{\delta \varphi}{\delta \eta}, \qquad (3)$$

where e is electron charge, V is supercell volume, and c is the supercell height. Note that we restrict ourselves to the diagonal e_{33} parameter calculations since (a) it is experimentally the mostly reliably measured parameter, and (b) the symmetry of the supercell in this particular case is preserved during piezoelectric constant calculations that allows us to estimate the piezoelectric constant e_{33} for any tetragonal symmetry without the center of inversion considered in this paper. In general estimates of other piezoelectric tensor elements in ferroelectrics with several phases, e.g. BTO, according to algorithm implemented in CRYSTAL17 [41] are limited only to the energetically most stable phase since unstrained geometry should be the lowest in energy. Otherwise the structural deformation during strain modeling might lead to an undefined situation, when the strained system is in a state with a lower symmetry and energy than the unstrained one.

The maximal strain values, η, used in the calculations must be chosen with a care. For a large m/M, when superlattice is close to a pseudo-cubic phase, excessive compressive strain in the [001] direction may force the system to swap the dipole orientation, that biases the calculated piezoelectric constant. In most calculations, we set the symmetric Lagrangian elastic tensor component with indexes $(3,3)$ to $\eta = 0.001$ (ELASTIC). In very demanding cases, for $m/M = 30/32$ in $P4$ model, we calculated the piezoelectric coefficient using a single deformation, i.e. by applying the smallest tensile strain of 0.0005. In order to compare accurately systems with close energies (including strained geometries), we used a FIXINDEX setting [41].

4 Simulation results

4.1 Bulk STO and BTO crystals

Let us test both $P4mm$ and $P4$ superlattice models in the limits of pure bulk STO and bulk BTO perovskites and verify that simulations lead to experimentally established perovskite phases. Therefore we need to consider both bulk STO and BTO perovskites in each of the four possible cases: in a single cubic ($Pm\bar{3}m$) and three tetragonal ($I4/mcm$, $P4mm$ and $P4$) symmetries, Table (1).

(i) Our *gedankenexperiment* with STO in the tetragonal $P4mm$ symmetry leads to a trivial result. After full structure optimization, STO remains in a cubic $Pm\bar{3}m$ phase since within the $P4mm$ symmetry rotations of oxygen octahedra are forbidden, see Table (1). Both lattice constant, a_0, and *tetragonality parameter*, $(c_0/a_0)-1$, of $P4mm$ coincide with those of a cubic phase $Pm\bar{3}m$

within the numerical accuracy of the order of 10^{-3} Å. Similarly, the atomic displacements agree with the corresponding cubic ones ($\delta^X=0$) and the total energy difference between both structures, ΔE^{ATO}, is zero.

As expected, STO in the $I4/mcm$ symmetry is energetically more favorable (by $\Delta E^{ATO} = -0.76$ meV per formula unit) comparing to the cubic one, Table (1). The gain is due to oxygen octahedra, TiO_6, antiphase rotation (AFD_z displacements), that is reflected in O_{II} coordinate, $\delta^{O_{II}}$, displacement from pseudo-cubic zero value according to [49]†

$$\theta_z^{TiO_6} = \arctan(4\delta^{O_{II}}) \qquad (4)$$

and slight increase of tetragonality. It was suggested in Ref. 48 that for a regular oxygen octahedra with all equal edges the ratio c_0/a_0 should be equal to $1/\cos(\theta_z^{TiO_6})$ that would allow to describe STO geometry using a single parameter. However, in our bulk calculations the out of plane edges of octahedra are 10^{-3} Å longer than the in-plane edges, and the suggested relation does not hold. Thus, our calculations support the two parameter STO phase transition model [49,50].

Lastly, $P4$ is the lowest tetragonal space group that allows both oxygen octahedra rotation (AFD_z displacements) and atomic [001] displacements (FE_z displacements), see Fig. 1. When STO compound is considered in such $P4$ symmetry, the geometry optimization converges to the tetragonal phase $I4/mcm$ (within the accuracy of 10^{-3} Å). Note that the oxygen octahedra rotation angles in $P4$ model vary separately in each layer, see Table (1), contrary to the $I4/mcm$, and therefore all rotation angles agree well. Moreover, the atomic [001] displacements are absent in both $P4$ and $I4/mcm$ models.

As is well known, the piezoelectric effect is absent in centrosymmetric space groups (with the center of inversion, e.g., $Pm\bar{3}m$ and $I4/mcm$). Despite the fact that we consider STO in space groups $P4mm$ and $P4$ that have no center of inversion, our calculations in agreement with experiments demonstrate that the piezoelectric effect in bulk STO is absent, $e_{33} = 0.0$ C/m^2, see Table (1).

By comparison with experiments, Table (2), the STO pseudo-cubic lattice constant, a_0, is slightly underestimated in the $Pm\bar{3}m$ and $I4/mcm$ structures. Oxygen octahedra rotation angle as well as tetragonality, however, is approximately twice larger for $I4/mcm$, when comparing with the experiment at 77 K. (Note however that at lower temperatures (4.2 K) rotation angle increases till 2.1° [48] which makes agreement better). The agreement between the calculated and experimental band gaps is also good, as well as with with recent first-principles studies of STO [36,49,51,52]. Note also that antiferrodistortive phase with ferroelectric displacements was predicted theoretically in thin STO films [53].

(ii) Another *gedankenexperiment* with BTO in the $I4/mcm$ symmetry converges to the $Pm\bar{3}m$ phase (since displacement of atoms in the [001] direction is forbidden and rotation of oxygen octahedra are energetically unfavorable in $I4/mcm$, Fig. 1). In both

---

† See note for $I4/mcm$ space group in Fig. 1.

Table 1 Theoretically calculated pseudo-cubic structural parameters (a_0 and c_0), displacements from pseudo-cubic $Pm\bar{3}m$ positions if allowed by symmetry (δ in fractional units, see Fig. 1, and $\delta_i^A \equiv 0$), octahedral rotation angle ($\theta_z^{TiO_6}$), total energy difference per formula unit (ΔE^{ATO}, where $Pm\bar{3}m$ energy is set as the zero energy level 0), band gap (E_g) and total proper direct piezoelectric (stress) tensor coefficient (e_{33}) for STO and BTO bulk crystals in different space groups (SG). Subscript indexes at δ denote (x,y,z) components, see Fig.1

SG	a_0 (Å)	$(c_0/a_0)-1$	δ^{Ti}	δ^{O_I}	$\delta^{O_{II}}$	$\theta_z^{TiO_6}$ (°)	ΔE^{ATO} (meV)	E_g (eV)	e_{33} (C/m²)
STO:									
$Pm\bar{3}m$(#221)	3.884	0	-	-	-	-	"0"	3.36	-
$P4mm$(#99)	3.884	0.000	0.000_z	0.000_z	0.000_z	-	0.00	3.36	0.0
$I4/mcm$(#140)	3.880	0.002	-	-	$0.014_{x,y}$	3.2	-0.76	3.39	-
$P4$(#75)	3.881	0.002	$0.000_z{}^a$	$0.000_z{}^a$	$+0.014_x, -0.014_y, 0.000_z{}^a$ $-0.014_x, +0.014_y, 0.000_z{}^a$	3.1 -3.1	-0.76	3.39	0.0
BTO:									
$Pm\bar{3}m$(#221)	3.975	0	-	-	-	-	"0"	3.20	-
$P4mm$(#99)	3.962	0.022	0.018_z	-0.028_z	-0.015_z	-	-19.61	3.26	4.3
$I4/mcm$(#140)	3.975	0.000	-	-	$0.000_{x,y}$	0.0	$+0.03$	3.20	-
$P4$(#75)	3.962	0.022	$0.017_z{}^a$	$-0.029_z{}^a$	$0.000_x, 0.000_y, -0.016_z{}^a$ $0.000_x, 0.000_y, -0.016_z{}^a$	0.0 0.0	-19.65	3.26	4.3

^{a} *The fractional coordinate δ_z of the space group $P4$ is scaled to a single unit cell height (multiplied by 2) for comparison with $P4mm$ data.*

Table 2 Experimental pseudo-cubic structural parameters (a_0 and c_0), displacements from pseudo-cubic $Pm\bar{3}m$ positions if allowed by symmetry (δ in fractional units, see Fig. 1), octahedral rotation angle ($\theta_z^{TiO_6}$), band gap (E_g, $\|$ and $\perp$ stand for light polarized parallel and perpendicular to the ferroelectric z-axis, respectively) and the total proper direct piezoelectric (stress) tensor coefficient (e_{33}) for STO and BTO bulk crystals in different SG [33,37,48]

SG	a_0 (Å)	(c_0/a_0)-1	δ^{Ti}	δ^{O_I}	$\delta^{O_{II}}$	$\theta_z^{TiO_6}$ (°)	E_g (eV)	e_{33} (C/m²)
STO:								
$Pm\bar{3}m$(#221)	3.905 (293K)	0	-	-	-	-	3.40 (296K)	-
$I4/mcm$(#140)	≈3.905	≈0.001	-	-	$0.006_{x,y}$ (77K)	1.4 (77K)	3.43 (77K)	-
BTO:								
$Pm\bar{3}m$(#221)	3.996 (393K)	0	-	-	-	-	3.25 (403K)	-
$P4mm$(#99)	3.992 (293K)	0.011 (293K)	0.0135_z (295K)	-0.025_z (295K)	-0.015_z (295K)	-	$3.38^\|$, $3.27^\perp$ (293K)	6.7 (296K)

symmetries piezoelectric constants are zero, due to the presence of the center of inversion.

The tetragonal $P4mm$ symmetry is energetically more favorable for BTO than cubic $Pm\bar{3}m$. This is related to the cation and anion movement in opposite [001] directions from pseudo-cubic positions and appearance of tetragonality. The BTO lattice tetragonality is an order of magnitude larger than that of the STO in $I4/mcm$ symmetry, Table 1.

Lastly, BTO modeling in the $P4$ symmetry shows that lattice constant and tetragonality converge to the $P4mm$ phase, within high accuracy of 10^{-3} Å, Table 1. In this case displacements from pseudo-cubic positions in [001] direction, absence of oxygen octahedra rotation, energy gain comparing to cubic $Pm\bar{3}m$ symmetry, and band gap agrees well with the $P4mm$ model, Table 1.

Similarly to bulk STO case, the piezoelectric effect is absent for BTO in $Pm\bar{3}m$ and $I4/mcm$ symmetries due to the presence of center of inversion, Table 1. In turn, in both other $P4mm$ and $P4$ symmetries we obtain equal piezoelectric coefficient, e_{33}, estimates, within the accuracy of 10^{-1} C/m², Table 1.

The BTO pseudo-cubic lattice constant, a_0, in both $Pm\bar{3}m$ and $P4mm$ symmetries is slightly underestimated, while tetragonality of $P4mm$ is twice larger, comparing to experiment, Table 2. The fractional atomic displacements, band gap and piezoelectric constant agrees well with experiments and previous first-principle

studies [36,38,44,54–56]. Moreover, the vibrational analysis of pure BTO and STO crystals not present here were in complete agreement with earlier results [36,38].

Thus, our bulk STO and BTO calculations demonstrate that the tetragonal STO_m/BTO_{M-m} superlattice could be simulated using two models. The first one, that is based on STO_m/BTO_{M-m} calculations within $P4mm$ symmetry, in the limiting cases of bulk STO and BTO structures, leads to the formal cubic STO ($Pm\bar{3}m$) and tetragonal BTO ($P4mm$) symmetries, respectively. The second model, on the basis of tetragonal STO_m/BTO_{M-m} superlattice in $P4$ symmetry, in the limiting cases of bulk STO and BTO, in turn gives the tetragonal STO ($I4/mcm$) and BTO ($P4mm$) symmetries, respectively.

4.2 $P4mm$ model of STO_m/BTO_{M-m} superlattice

Let us consider now the STO_m/BTO_{M-m} superlattice within the $P4mm$ model. The direct piezoelectric constant e_{33} increases with the number of STO layers, Fig. 3a. However, after reaching a maximum at $m/M = 14/16 \sim 0.88$, addition of one more STO layer (ratio of $15/16 \sim 0.94$) leads to the abrupt disappearance of piezoelectric effect (we have confirmed this behavior also for $m/M = 30/32 \sim 0.94$). The piezoelectric coefficients for a various number of total layers, M, but identical ratios, m/M, are similar for $m/M \leq 0.75$. Strong dependence on M is observed at higher ra-
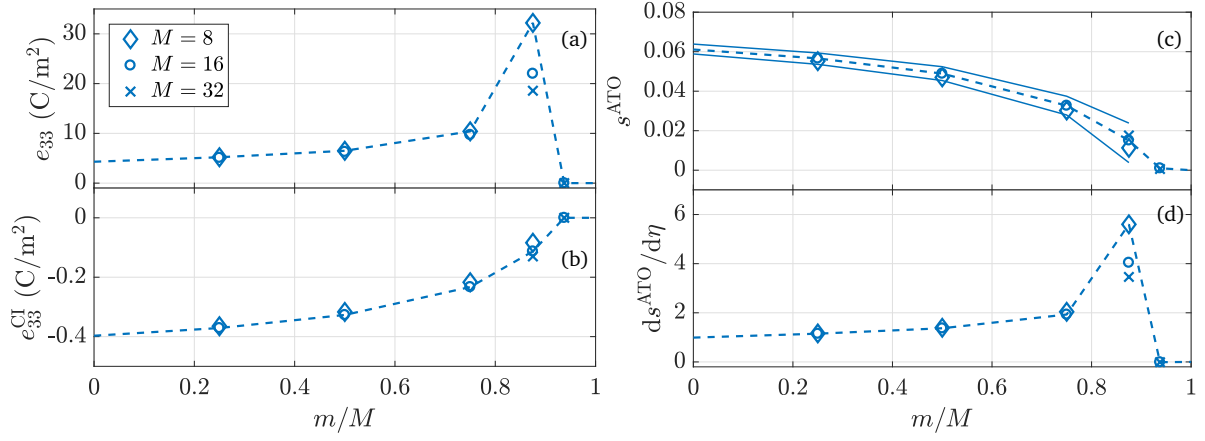
Fig. 3 STO$_m$/BTO$_{M-m}$ superlattice in the $P4mm$ model. a) Direct proper piezoelectric constant, e_{33} (including atomic position relaxation) and b) "clamped-ion" contribution, e_{33}^{CI} (in the absence of atomic position relaxation), respectively. c) Displacement between AO$_I$ and TO$_{II}$ planes, s^{ATO}, see text for details. The continues lines show variation of s^{ATO} under compressive and tensile dimensionless strain, $\eta = 0.0025$. d) Derivative of, s^{ATO}, with respect to strain, η. The dashed lines are guides for the eye. The total number of layers M is given in the legend.
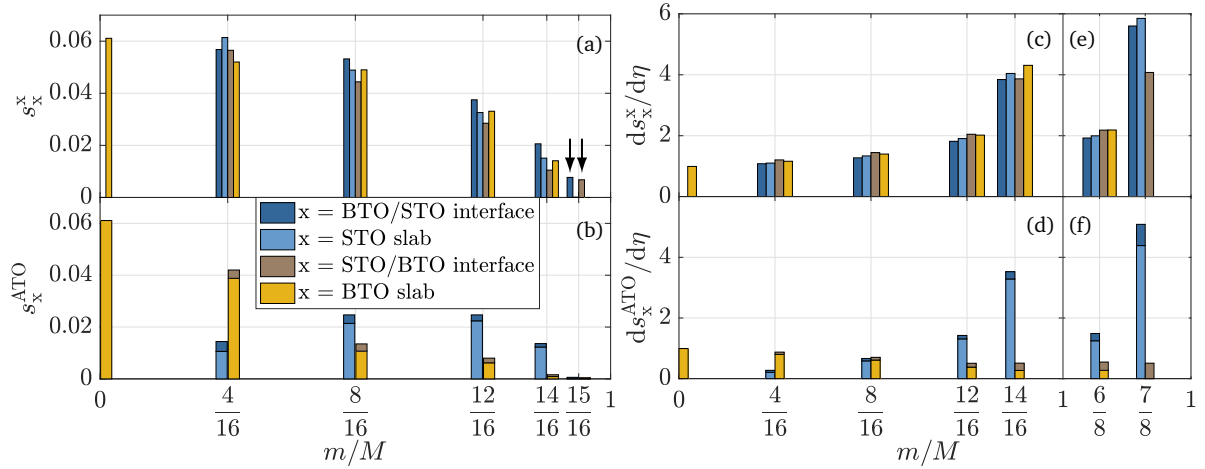
Fig. 4 Decomposition of Figs. 3c,d into contributions. (a,b) Displacement, s^{ATO}, (see Fig. 3c) decomposition into contributions, s_x^y. Subscript, x, indicates the contribution of either BTO/STO interface, STO slab, STO/BTO interface or BTO slab. Superscript, y, denotes normalization to a single formula unit (ATO) or to single layer (from BTO/STO interface, STO slab, STO/BTO interface or BTO slab), respectively. (c-f): Displacement derivative, ds^{ATO}/dη (see Figs. 3d) decomposition into contributions, ds_x^y/dη. Total number of layers (a-d) $M = 16$ and (e-f) $M = 8$, respectively.

tio $m/M \sim 0.88$. At this ratio for $M = 8$ layer model ($m/M = 7/8 \sim 0.88$) we find $\sim$ 6-fold increase of e_{33}, while for $M = 16$ and 32 superlattices piezoelectric constant decreases and saturates to only $\sim$ 4-fold increase, comparing to its bulk BTO value, Fig. 3a. The purely electronic contribution to piezoelectric constant (without atomic relaxations) is calculated using "clamped-ion" approximation, e_{33}^{CI}, see Fig. 3b. It is an order of magnitude smaller than e_{33} for bulk BTO and tends to zero with an increase of the number of STO layers. The electronic contribution alone cannot explain an enhancement of e_{33} in STO$_m$/BTO$_{M-m}$ with the number of STO layers, similarly to Ba$_{(1-x)}$Sr$_x$TiO$_3$ solid solution[6].

In order to relate the atomic relaxation effect with piezoelectric constant, let us note that piezoelectric constant, e_{33}, is related to the variation of polarization, P, under strain, η, in [001] direction, Eq. (2). In turn polarization, P, is proportional to a total dipole moment p in [001] direction, $P = V^{-1}p$, and the dipole moment is proportional to a displacement, s, that separates charges (under assumption that separated charges for all dipoles are similar and

weakly affected by strain values used in our calculations) within the lattice volume, V. Thus, let us define the total displacement in [001] direction s^{ATO} (displacement, from here on), as a sum of partial displacements between planes of AO$_I$, s^{AO_I}, and TO$_{II}$, $s^{TiO_{II}}$, (in fractional coordinates that for a convenience are normalized per a single ATO formula unit)

$$s^{ATO} = s^{AO_I} + s^{TiO_{II}}, \qquad (5)$$

see Fig 2a. According to the definition, s^{ATO} approaches zero when atoms tend to occupy their pseudo-cubic structure positions. Let us note that for bulk crystal the displacement in Eq. 5 could be estimated as

$$s^{ATO} = |\delta_z^A| + |\delta_z^{O_I}| + |\delta_z^{Ti}| + |\delta_z^{O_{II}}|, \qquad (6)$$

where z-displacements from pseudo-cubic $Pm\bar{3}m$ positions could be obtained from Table 1.

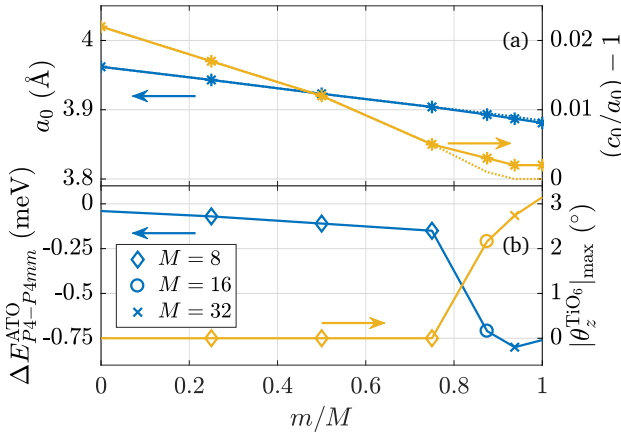Firstly, let us consider the displacement, s^{ATO}, in the absence

Fig. 5 a) In-plane lattice constant, a_0, and tetragonality dependence on the layer ratio, m/M, for the $P4mm$ (dashed lines) and $P4$ models (solid lines with stars). b) The energy difference, $\Delta E^{ATO}_{P4-P4mm}$, between superlattices in $P4$ and $P4mm$ models (per formula unit ATO) and maximal rotation angle of the oxygen octahedra in $P4$. Symbols denote total layer number, M, see Fig. 3.

of strain. With an increase of the number of STO layers, m, the displacement s^{ATO} decreases from the bulk BTO ($s^{ATO} = 0.061$, see Table 1) value to that in STO ($s^{ATO} = 0$), Fig. 3c.

Due to additivity of terms in Eq. (5), we can decompose the displacement s^{ATO} into four components describing contributions from BTO/STO interface layer, STO slab, STO/BTO interface layer and BTO slab, respectively, see Fig. 2a,

$$s^{ATO} = s^{ATO}_{BTO/STO} + s^{ATO}_{STO} + s^{ATO}_{STO/BTO} + s^{ATO}_{BTO}, \qquad (7)$$

that are normalized to an ATO formula unit, Eq. 7. The contribution of BTO slab displacements dominates for $m/M < 0.5$, Fig. 4b. For larger m/M ratios the STO slab displacements prevail, while interface effect remains small for all ratios that demonstrate piezoelectric effect. This behavior could be understood by introducing displacements normalized to a single (BTO/STO interface, $s^{BTO/STO}_{BTO/STO}$; STO slab, s^{STO}_{STO}; STO/BTO interface, $s^{STO/BTO}_{STO/BTO}$; and BTO slab, s^{BTO}_{BTO}) layer contributions. It can be shown, that the single layer displacement contribution to the displacement s^{ATO} is proportional just to the layer number in the superlattice

$$s^{ATO} = \frac{1}{M}s^{BTO/STO}_{BTO/STO} + \frac{m-1}{M}s^{STO}_{STO} + \frac{1}{M}s^{STO/BTO}_{STO/BTO} + \frac{M-m-1}{M}s^{BTO}_{BTO}. \qquad (8)$$

Single layer displacement representation, Eq. (8), demonstrates, that displacements in all single layers of BTO and STO as well as their interfaces are approximately equal, Fig. 4a. A remarkable behavior is observed for $m/M = 15/16 \sim 0.94$ ratio ($e_{33} = 0$ C/m^2) when there is a rumpling on both STO and BTO interfaces (marked with arrows in Fig. 4a), but the displacements in both STO and BTO slabs are absent ($s^{STO}_{STO} = s^{BTO}_{BTO} = 0$) indicating that both slabs are in a pseudo-cubic phase, Figs. 4a,b.

Secondly, let us consider compressively and tensilely strained superlattices. Then the displacement, s^{ATO}, decreases with the number of STO layers, however, in a non-proportional way, see solid lines in Fig. 3c. The displacement derivative with respect to a strain, $ds^{ATO}/d\eta$, behaves quantitatively similarly to e_{33},

Figs. 3a and d, that allows us to interpret the piezoelectric behavior in terms of displacements. More so, for $m/M = 7/8 \sim 0.88$ ratio the displacement derivative increases $\sim$ 6-fold comparing to the bulk BTO value, i.e., despite the small s^{ATO} value (the superlattice is close to the point where tetragonal phase stability decreases tending towards pseudo-cubic phase) the displacement variation, Δs^{ATO}, reaches maximum upon strain variation.

The displacement derivative could be partitioned into contributions using Eqs.(7–8), see Fig. 4c-f. When contributions are normalized per formula unit, the impact of BTO and STO layers decrease and increase with m/M ratio proportionally to the number of BTO and STO layers in the superlattice, respectively, Fig. 4d,f. In turn, contribution from single layers are similar, irrespectively of the layer position (STO slab, BTO slab, or STO and BTO interfaces), Fig. 4c,e. Let us now analyze the components for two identical ratios $m/M \sim 0.88$, but different total number of layers M, i.e., $m/M = 14/16$ and $7/8$, Fig. 4c-f, that lead to different piezoelectric constants $e_{33} = 22$ and 32 C/m^2, Fig. 3a, respectively. The BTO slab region is absent in the $M = 8$ layer superlattice, since there is just a single layer of BTO. In this case contribution from both single STO slab and BTO/STO interface layers are $\sim$ 30% larger than from STO/BTO interface, Fig. 4e.

For $P4mm$ group the in-plane lattice constant, a_0, decreases approximately linearly with the ratio, m/M, see dashed line in Fig. 5a. The tetragonality estimate also decreases with m/M and reaches zero value at the same $m/M \geq 15/16 \equiv 30/32 \sim 0.94$ ratios, when piezoelectric constant, e_{33}, becomes zero and superlattice becomes pseudo-cubic. Thus the absence of piezoelectricity could be explained by the recovery of the center of inversion in pseudo-cubic slabs.

4.3 $P4$ model of STO$_m$/BTO$_{M-m}$ superlattice

Similarly to $P4mm$ results discussed above, the direct piezoelectric constant e_{33} in $P4$ model increases with the number of STO layers m/M, Fig. 6a. The clamped-ion contribution e^{CI}_{33} is by an order of magnitude smaller than the piezoelectric constant for the bulk BTO and it tends to zero for the bulk STO, Fig. 6b. For small and average ratios, $m/M \leq 6/8 \sim 0.75$, the piezoelectric constant behaves similarly for both space groups, $P4mm$ and $P4$. However, for larger ratios, e.g., at $m/M = 30/32 \sim 0.94$ we observe a qualitatively different behavior. At this ratio e_{33} reaches maximum ($\sim$6-fold increase compared to the bulk BTO) in $P4$ model and shows clearly a ferroelectric behavior, while within $P4mm$ symmetry, the ferroelectric effect was already lost.

The displacement s^{ATO} decreases with m/M, Fig. 6c. However, the variation of the displacement under compressive and tensile strain increases with m/M, see solid lines in Fig. 6c, leading to a maximum of 6-fold increase of s^{ATO} derivative, Fig 6d. This increase correlates with the growth of direct piezoelectric coefficient in Fig. 6a.

Decomposition of the s^{ATO} into contributions from single STO and BTO slab layers and their interfaces (s^x_x, where x is STO, BTO, BTO/STO interface and STO/BTO interface) shows that all single layers contribute to s^{ATO} approximately equally, Fig. 7a. The contribution of single layers, s^x_x, to the total displacement, s^{ATO}, is
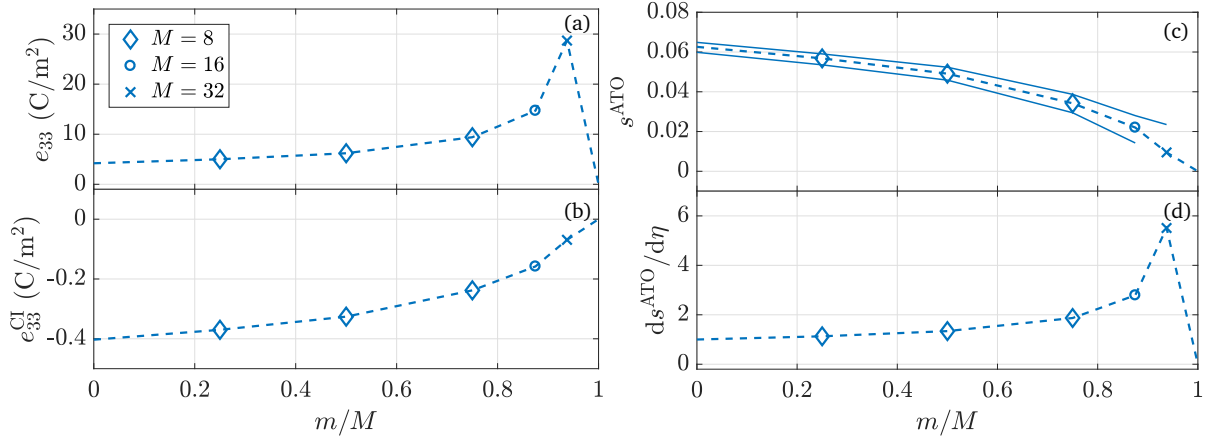
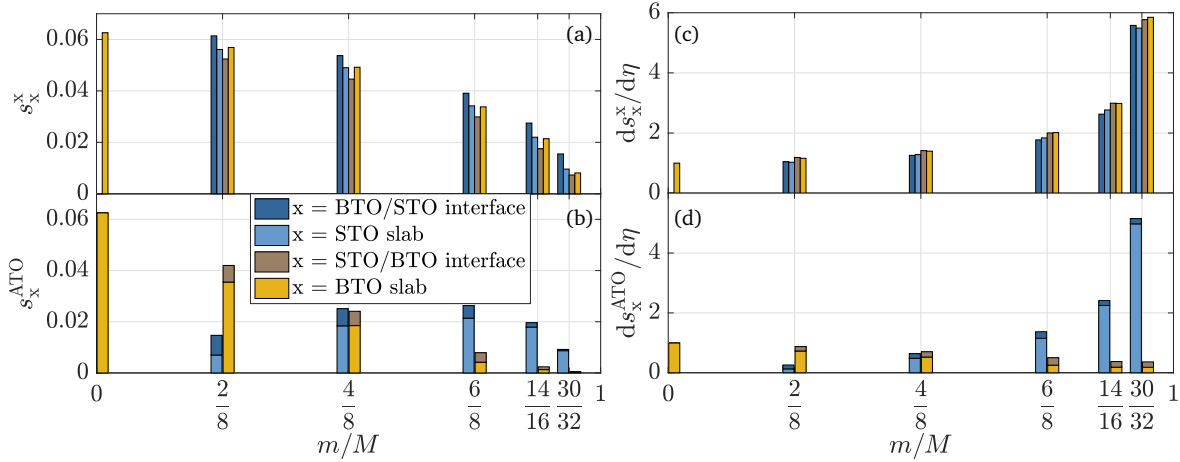**Fig. 6** STO$_m$/BTO$_{M-m}$ superlattice in $P4$ model, description identical to Fig. 3.

Fig. 7 Decomposition of Figs. 6c,d into contributions, description identical to Fig. 4a-d.

proportional to the number of these layers according to Eq. (8), see Fig. 7b. Contribution from BTO and STO layers is decreasing and increasing with m/M ratio, respectively.

The displacement derivative normalized to a single layer, $\mathrm{d}s_x^x/\mathrm{d}\eta$, is independent of the layer type and increases with the m/M ratio, see Fig. 7c. In turn the contribution to the total displacement derivative, $\mathrm{d}s^{ATO}/\mathrm{d}\eta$, is proportional to the number of individual layers, Fig. 7d. Since the largest piezoelectric constant, e_{33}, value is observed for $m/M = 30/32 \sim 0.94$ ratio, the dominant contribution to it comes from STO slab.

For $P4$ model the in-plane lattice constant, a_0, within the calculation accuracy coincides with that of $P4mm$ model and decreases approximately linearly with the STO and BTO layer ratio, m/M, see solid line with stars in Fig. 5a. The tetragonality estimate also decreases with m/M and saturates at bulk STO value for $m/M \geq 30/32 \sim 0.94$ ratios.

In all m/M ratio range the $P4$ superlattice model is energetically more favorable than the $P4mm$ one, Fig. 5b. The energy gain increases for $P4$ almost linearly up till $m/M \leq 0.75$, in the absence of oxygen octahedra rotation, Fig. 5b. For a larger ratios we observe a considerable energy gain for $P4$ model, that is accompanied with an increasing maximal oxygen octahedra rotation angle, Fig. 5b. The rotation of octahedra (in opposite directions in

neighboring layers) occurs only in STO slab, while octahedra in BTO slab doesn't rotate, Fig. 2b.

5 Discussion and Conclusions

Limiting ourselves to the tetragonal space group symmetry, we compared two models for STO$_m$/BTO$_{M-m}$ superlattices, which differ by symmetry, $P4mm$ and $P4$, respectively. For both models our calculations predict a considerable enhancement of the piezoelectric properties of STO$_m$/BTO$_{M-m}$ superlattices compared to the pure bulk BTO. Moreover, the largest effect is expected for low concentrations of BTO, i.e., in the predominantly STO-containing superlattices. With an increase of a number of STO layers, m, in superlattices we observed the change of: (i) the STO slab phases: either $P4mm \rightarrow Pm\bar{3}m$ or $P4mm \rightarrow P4 \rightarrow I4/mcm$ in $P4mm$ and $P4$ models, respectively; (ii) the BTO slab phases: $P4mm \rightarrow Pm\bar{3}m$, irrespectively of the model used. The largest piezoelectric coefficient is predicted in $P4mm$ and $P4$ models close to the point, where phase of superlattice changes from non-centrosymmetric to centrosymmetric, at ratio of STO/(STO+BTO) layer numbers $m/M = 7/8 \sim 0.88$ and $30/32 \sim 0.94$, respectively.

Our results suggest that piezoelectric effect in the superlattice arises as a collective FE$_z$ atomic displacements in all layers (both Ba and Sr slabs and both Ba/Sr and Sr/Ba interfaces) simultane-

ously and contribution to e_{33} from each individual layer is approximately equal. And, when the STO_m/BTO_{M-m} heterostructure is considered at the layer ratios leading to maximal e_{33} values, the main contribution to e_{33} comes from m STO layers just due to their increased number. Interface rumpling (boundary effect) is a key for induction of the FE_z displacements in STO slab. If STO slab exceeds a critical thickness, the rumpling at the interface albeit present triggers no FE_z displacements in STO and piezoelectric effect in both STO and BTO superlattice slabs disappears.

The calculations performed in the framework of tetragonal STO_m/BTO_{M-m} superlattice allow us also to interpret some basic experimental results. (i) Thus, the observed cooperative behavior between collective ionic displacements along the [001] axis in both STO and BTO slabs in ferroelectric regime support the conclusion[15] on a 'strong coupling between slabs' model rather than decoupled (BTO slab only polarization) model.

(ii) Our model puts a constrain on the symmetry of ferroelectric superlattice STO_m/BTO_{M-m} with ratio $m/M = 30/31 \sim 0.97$, which was experimentally synthesized and analyzed in Ref. 11. In our simulations, the $P4mm$ model becomes paraelectric already as $m/M \geq 15/16 \sim 0.94$ which contradicts superlattice ferroelectric behavior found experimentally. However, our $P4$ model still remains ferroelectric at ratio $m/M = 30/32 \sim 0.94$ (and demonstrates oxygen octahedra rotation) in agreement with experimental data[11].

(iii) The very fact that inclusion of the octahedra rotations in $P4$ model allows the ferroelectric mode to survive at larger STO ratios ($m/M = 30/32 \sim 0.94$) than in $P4mm$ model indicates that in our superlattice model the AFD_z mode cooperate with the FE_z mode and thus promotes the ferroelectric behavior, similarly to Ref. 57 (also at much smaller octahedra rotation angles).

In order to analyze AFD_z mode in the absence of FE_z mode, we have simulated STO_m/BTO_{M-m} superlattice up till $m/M \leq 12/16 \sim 0.75$ ratio in $I4/mcm$ model. We have observed no rotation of oxygen octahedra in a STO slab, that indicate that BTO slab with its non-rotated oxygen octahedra reacts as a resisting force at STO/BTO slab interface. This trend explains the octahedra rotation (AFD_z displacement) behavior in $P4$ model, where rotation occurs only in a STO slab (rotation angle increases with the distance from interface) and for large $m/M \geq 14/16 \sim 0.88$ ratios, see Figs. 2b and 5b. Our conclusion addresses different situation than that considered in Ref. 58, where antiferrodistortive and ferroelectric modes trend to compete with each other in the bulk.

Conflicts of interest

There are no conflicts to declare.

Acknowledgments

References

1 J.-H. Lee, J. Kim, T. Y. Kim, M. S. Al Hossain, S.-W. Kim and J. H. Kim, *J. Mater. Chem. A*, 2016, **4**, 7983–7999.

2 Y. Zhang, C. K. Jeong, T. Yang, H. Sun, L.-Q. Chen, S. Zhang, W. Chen and Q. Wang, *J. Mater. Chem. A*, 2018, **6**, 14546–14552.

3 B. Jaffe, W. R. Cook and H. Jaffe, *Piezoelectric Ceramics*, Academic Press, 1971.

4 M. M. Kržmanc, H. Uršič, A. Meden, R. C. Korošec and D. Suvorov, *Ceram. Int.*, 2018, **44**, 21406–21414.

5 M. Acosta, N. Novak, V. Rojas, S. Patel, R. Vaish, J. Koruza, G. A. Rossetti and J. Rödel, *Appl. Phys. Rev.*, 2017, **4**, 041305.

6 L. L. Rusevich, G. Zvejnieks, A. Erba, R. Dovesi and E. A. Kotomin, *J. Phys. Chem. A*, 2017, **121**, 9409–9414.

7 L. L. Rusevich, G. Zvejnieks, E. A. Kotomin, M. M. Kržmanc, A. Meden, Š. Kunej and I. D. Vlaicu, *J. Phys. Chem. C*, 2019, **123**, 2031–2036.

8 L. L. Rusevich, G. Zvejnieks and E. A. Kotomin, *Solid State Ionics*, 2019, **337**, 76–81.

9 D. G. Schlom, L.-Q. Chen, C.-B. Eom, K. M. Rabe, S. K. Streiffer and J.-M. Triscone, *Annu. Rev. Mater. Res.*, 2007, **37**, 589–626.

10 A.-B. Posadas, M. Lippmaa, F. J. Walker, M. Dawber, C. H. Ahn and J.-M. Triscone, in *Physics of Ferroelectrics. Topics in Applied Physics*, Springer, Berlin, Heidelberg, 2007, vol. 105, pp. 219–304.

11 D. G. Schlom, L.-Q. Chen, C. J. Fennie, V. Gopalan, D. A. Muller, X. Pan, R. Ramesh and R. Uecker, *MRS Bull.*, 2014, **39**, 118–130.

12 D. A. Tenne *et al.*, *Science*, 2006, **313**, 1614–1616.

13 G. Liu, Y. Wang, B. Zou, W. Liang, N. M. Alford, D. W. McComb and P. K. Petrov, *J. Phys. Chem. C*, 2016, **120**, 16681–16686.

14 V. Železný, O. Caha, A. Soukiassian, D. G. Schlom and X. X. Xi, *Phys. Rev. B*, 2017, **95**, 214110.

15 B. Bein, H.-C. Hsing, S. J. Callori, J. Sinsheimer, P. V. Chinta, R. L. Headrick and M. Dawber, *Nat. Commun.*, 2015, **6**, 10136.

16 H. Tabata, H. Tanaka and T. Kawai, *Appl. Phys. Lett.*, 1994, **65**, 1970–1972.

17 D. O'Neill, R. M. Bowman and J. M. Gregg, *Appl. Phys. Lett.*, 2000, **77**, 1520–1522.

18 G. Catalan, D. O'Neill, R. M. Bowman and J. M. Gregg, *Appl. Phys. Lett.*, 2000, **77**, 3078–3080.

19 A. Q. Jiang, J. F. Scott, H. Lu and Z. Chen, *J. Appl. Phys.*, 2003, **93**, 1180–1185.

20 S. Ríos, A. Ruediger, A. Q. Jiang, J. F. Scott, H. Lu and Z. Chen, *J. Phys.: Condens. Matter*, 2003, **15**, L305–L309.

21 V. Železný, A. Soukiassian, D. G. Schlom and X. X. Xi, *J. Appl. Phys.*, 2014, **115**, 184102.

22 L. Kim, J. Kim, Y. S. Kim, D. Jung, N. Park and J. Lee, *Integr. Ferroelectr.*, 2002, **50**, 219–228.

23 J. Kim, Y. Kim, Y. S. Kim, J. Lee, L. Kim and D. Jung, *Appl. Phys. Lett.*, 2002, **80**, 3581–3583.

24 L. Kim, D. Jung, J. Kim, Y. S. Kim and J. Lee, *Appl. Phys. Lett.*, 2003, **82**, 2118–2120.

25 R. R. Das, Y. I. Yuzyuk, P. Bhattacharya, V. Gupta and R. S. Katiyar, *Phys. Rev. B*, 2004, **69**, 132302.

26 A. Soukiassian *et al.*, *J. Mater. Res.*, 2008, **23**, 1417–1432.

27 J. Ravichandran *et al.*, *Nat. Mater.*, 2013, **13**, 168–172.

28 J. B. Neaton and K. M. Rabe, *Appl. Phys. Lett.*, 2003, **82**, 1586–1588.

29 K. Johnston, X. Huang, J. B. Neaton and K. M. Rabe, *Phys. Rev. B*, 2005, **71**, 100103.

30 L. Kim, J. Kim, D. Jung, J. Lee and U. V. Waghmare, *Appl. Phys. Lett.*, 2005, **87**, 052903.

31 A. I. Lebedev, *J. Adv. Dielectr.*, 2012, **02**, 1250003.

32 J. H. Lee, J. Yu and U. V. Waghmare, *J. Appl. Phys.*, 2009, **105**, 016104.

33 M. Adachi *et al.*, in *Landolt-Börnstein - Group III Condensed Matter*, ed. Y. Shiozaki, E. Nakamura and T. Mitsui, Springer-Verlag Berlin Heidelberg, 2001, vol. 36A1.

34 H. Bärnighausen, *MATCH Commun. Math. Comput. Chem.*, 1980, **9**, 139–175.

35 M. I. Aroyo, J. M. Perez-Mato, D. Orobengoa, E. Tasci, G. de la Flor and A. Kirov, *Bulg. Chem. Commun.*, 2011, **43**, 183–197.

36 R. A. Evarestov, E. Blokhin, D. Gryaznov, E. A. Kotomin and J. Maier, *Phys. Rev. B*, 2011, **83**, 134108.

37 G. Shirane and Y. Yamada, *Phys. Rev.*, 1969, **177**, 858–863.

38 R. A. Evarestov and A. V. Bandura, *J. Comput. Chem.*, 2012, **33**, 1123–1130.

39 G. Shirane, H. Danner and R. Pepinsky, *Phys. Rev.*, 1957, **105**, 856–860.

40 R. Dovesi *et al.*, *Wiley Interdiscip. Rev. Comput. Mol. Sci.*, 2018, **8**, e1360.

41 R. Dovesi *et al.*, *CRYSTAL17 User's Manual*, University of Torino, Torino, 2017.

42 T. Bredow, K. Jug and R. A. Evarestov, *Phys. Status Solidi B*, 2006, **243**, R10–R12.

43 S. Piskunov, E. Heifets, R. Eglitis and G. Borstel, *Comput. Mater. Sci.*, 2004, **29**, 165–178.

44 D. I. Bilc, R. Orlando, R. Shaltaf, G.-M. Rignanese, J. Íñiguez and P. Ghosez, *Phys. Rev. B*, 2008, **77**, 165107.

45 H. J. Monkhorst and J. D. Pack, *Phys. Rev. B*, 1976, **13**, 5188–5192.

46 A. Erba, D. Caglioti, C. M. Zicovich-Wilson and R. Dovesi, *J. Comput. Chem.*, 2017, **38**, 257–264.

47 J. Baima, A. Erba, L. Maschio, C. M. Zicovich-Wilson, R. Dovesi and B. Kirtman, *Z. Phys. Chem.*, 2016, **230**, 719–736.

48 H. Unoki and T. Sakudo, *J. Phys. Soc. Jap.*, 1967, **23**, 546–552.

49 A. Erba, K. E. El-Kelany, M. Ferrero, I. Baraille and M. Rérat, *Phys. Rev. B*, 2013, **88**, 035102.

50 A. Heidemann and H. Wettengel, *Z. Physik*, 1973, **258**, 429–438.

51 E. Heifets, E. Kotomin and V. A. Trepakov, *J. Phys.: Condens. Matter*, 2006, **18**, 4845–4851.

52 C. E. Ekuma, M. Jarrell, J. Moreno and D. Bagayoko, *AIP Adv.*, 2012, **2**, 012189.

53 E. Blokhin, R. A. Evarestov, D. Gryaznov, E. A. Kotomin and J. Maier, *Phys. Rev. B*, 2013, **88**, 241407(R).

54 J. J. Wang, F. Y. Meng, X. Q. Ma, M. X. Xu and L. Q. Chen, *J. Appl. Phys.*, 2010, **108**, 034107.

55 A. Mahmoud, A. Erba, K. E. El-Kelany, M. Rérat and R. Orlando, *Phys. Rev. B*, 2014, **89**, 045103.

56 E. Goh, L. Ong, T. Yoon and K. Chew, *Comput. Mater. Sci.*, 2016, **117**, 306–314.

57 T. Gu, T. Scarbrough, Y. Yang, J. Íñiguez, L. Bellaiche and H. J. Xiang, *Phys. Rev. Lett.*, 2018, **120**, 197602.

58 W. Zhong and D. Vanderbilt, *Phys. Rev. Lett.*, 1995, **74**, 2587–2590.